Semiclassical wave packet study of anomalous isotope effect in ozone formation

Evgeny Vetoshkin and Dmitri Babikov[a)]
Chemistry Department, Wehr Chemistry Building, Marquette University, Milwaukee, Wisconsin 53201-1881, USA

(Received 12 June 2007; accepted 7 August 2007; published online 18 October 2007)

We applied the semiclassical initial value representation method to calculate energies, lifetimes, and wave functions of scattering resonances in a two-dimensional potential for $O+O_2$ collision. Such scattering states represent the metastable O_3^* species and play a central role in the process of ozone formation. Autocorrelation functions for scattering states were computed and then analyzed using the Prony method, which permits one to extract accurate energies and widths of the resonances. We found that the results of the semiclassical wave packet propagation agree well with fully quantum results. The focus was on the $^{16}O^{16}O^{18}O$ isotopomer and the anomalous isotope effect associated with formation of this molecule, either through the $^{16}O^{16}O+^{18}O$ or the $^{16}O+^{16}O^{18}O$ channels. An interesting correlation between the local vibration mode character of the metastable states and their lifetimes was observed and explained. New insight is obtained into the mechanism by which the long-lived resonances in the delta zero-point energy part of spectrum produce the anomalously large isotope effect. © *2007 American Institute of Physics*. [DOI: 10.1063/1.2778432]

I. INTRODUCTION

Ozone (O_3) is formed in the stratosphere as a product of the following recombination reaction:

$$O + O_2 + M \Rightarrow O_3 + M, \tag{1}$$

where M can be any atmospheric atom or molecule.[1] One possible mechanism for this reaction is through energy transfer (Lindemann),[2–4]

$$O + O_2 \leftrightarrow O_3^*, \tag{2}$$

$$O_3^* + M \rightarrow O_3 + M. \tag{3}$$

This mechanism assumes formation of long-lived metastable complexes O_3^* that can decay or be quenched into stable O_3 molecules by collisions with M.

Oxygen has three stable isotopes: ^{16}O, ^{17}O, and ^{18}O. Although the lightest isotope ^{16}O is dominant in the atmosphere, the stratospheric ozone shows anomalously large (up to 40%) enrichments in the heavy isotopes of oxygen relative to the oxygen from which it is formed.[5–7] It is also well established that the rate of the ozone forming reaction is very sensitive to the isotopic composition.[8] For example, if we consider an asymmetric isotopomer of ozone, $^{16}O^{16}O^{18}O$, it is produced mainly by two "attachment" reactions,

$$^{16}O + {}^{16}O^{18}O \rightarrow {}^{16}O^{16}O^{18}O \leftarrow {}^{16}O^{16}O + {}^{18}O. \tag{4}$$

In the experiment the ratio of the third order reaction rate coefficients for these two processes, $R=\kappa_{1616+18}/\kappa_{16+1618}$, shows no dependence on the mass or chemical nature of the third body M,[1] but it exhibits a very large isotope effect:[8] $R_{exp} \approx 0.63$.

Despite a significant amount of experimental[5–10] and theoretical[11–29] work devoted to ozone formation, a complete theoretical picture of this phenomenon is still missing. Marcus and co-workers[12,14] were the first to reproduce experimental data within the framework of the empirically adjusted RRKM approach, leaving a number of crucial dynamics questions open. The first reactive scattering calculations carried out by Babikov *et al.*[18–20] demonstrated that this phenomenon has an essentially quantum mechanical origin. It was shown that the anomalous isotope effect in the ozone forming reactions can be explained by the presence of a large number of scattering resonances in a narrow energy range *between* the zero-point energies (ZPEs) of two entrance channels in the reaction (4). Schinke *et al.*[24,25] found an ingenious way to mimic this quantum ΔZPE effect within the framework of classical trajectory simulations by artificially "lifting" the asymptotic value of interaction potential in one of the channels. The quantum scattering studies of state-to-state transitions during the stabilization step (3) were reported by Charlo and Clary[16] and by Xie and Bowman[28] and have shown that the low-lying metastable states are indeed important for the isotope dependence of the ozone formation rates. However, due to the extreme complexity of fully quantum mechanical calculations, all the quantum scattering studies reported to date[16,18–20,28] have been restricted to various approximations and have not achieved a complete solution of the problem.

One alternative to the fully quantum calculations is the time-dependent semiclassical wave packet method,[30–33] also known as the Herman-Kluk propagator or the initial value representation (IVR) method.[34–36] It is well known that this approach reproduces the quantum ZPE[36,37] and can be used to describe bound states in strongly anharmonic potentials.[38,39] Grossmann used this method to calculate life-

[a)]Author to whom correspondence should be addressed. Electronic mail: dmitri.babikov@mu.edu

times and energies of several metastable states for collinear $H_3^* \rightarrow H+H_2$ decay in a two-dimensional (2D) potential energy surface (PES).[39] Note that since the PES for H_3 is repulsive and the metastable states are short lived (τ=0.02–0.08 ps), the propagation time in his calculations did not exceed 0.13 ps.

The ozone forming reaction is much more complicated to treat because the ozone PES has a deep attractive well ($D \approx 1.13$ eV) and accommodates a number of scattering resonances with lifetimes on order of τ=100 ps.[18] We found that in order to accurately characterize such long-lived resonances (using the Prony algorithm, see Sec. III below) propagation of the initial wave packet for at least ~4 ps was necessary, but the long time propagation is known to be a tough task for the IVR due to emergence of chaotic trajectories.[36,38] In our previous paper[29] we successfully applied the IVR approach to characterize long-lived resonances in a one-dimensional potential representing the minimum energy path for reaction (2). Here we build upon that work and extend our methodology onto a 2D case which allows us to study simultaneously two isotopic compositions of the reactants in reaction (4) and to explore the associated isotope effect. It should be emphasized that the ΔZPE effect is essentially a multichannel phenomenon and considering a 2D PES with two entrance channels is necessary and sufficient to observe it. Indeed, on a 2D PES introduced in the next section one entrance channel correlates with the left side of reaction (4), where the ZPE is determined by the mass of heavier diatomic reactant $^{16}O^{18}O$, while the other channel correlates with right side of the reaction (4), where the ZPE is determined by the mass of the lighter diatomic reactant $^{16}O^{16}O$. This gives us the $\Delta ZPE = ZPE_{1616} - ZPE_{1618}$.

This paper is organized as follows: Section II describes the model PES used in this study, outlines the semiclassical IVR method and the procedure for calculating the autocorrelation functions; analysis of the autocorrelation functions and properties of the scattering resonances are presented in Sec. III; kinetics of the recombination reactions and the isotope effect are discussed in Sec. IV; conclusions are given in Sec. V.

II. PES AND THE PROPAGATION METHOD

The main focus of this paper is on the application of the semiclassical methodology to the characterization of scattering resonances and description of the ΔZPE effect. To simplify this task as much as possible we have chosen to sacrifice accuracy of the potential (to some extent) and used an approximate 2D PES which describes semiquantitatively all major features of the ozone molecule. The emphasis is on an accurate description of the ΔZPE value and of the PES behavior in the channel regions because, as will be seen in the next section, those regions are most important for description of the metastable ozone states. Our PES is analytical, based on the Morse oscillator functions, and also includes several fine corrections,

$$V(r_1,r_2) = -D_0 + D[1-e^{-a(r_2)(r_1-r_e(r_2))}]^2 + D[1-e^{-a(r_1)(r_2-r_e(r_1))}]^2 + V_{vdW}(r_1) + V_{vdW}(r_2) + V_{inf}(r_1,r_2). \quad (5)$$

The minimum energy point of our PES is at $r_1=r_2=r_e=2.394$ a.u. which is very close to experimental value of 2.405 a.u. for the equilibrium bond lengths in O_3.[40] Vibrational frequencies for the symmetric and antisymmetric stretch normal modes calculated using our PES for $^{16}O_3$ are equal to 1100.4 and 1000.2 cm^{-1}, respectively, and these numbers are close to two corresponding fundamental vibration frequencies in ozone: 1101.9 and 1043.9 cm^{-1}.[22] (Using masses of the $^{16}O^{16}O^{18}O$ isotopomer the two calculated frequencies are 1083.6 and 987.1 cm^{-1}, respectively.) As one of the bonds is stretched and the shape of O_3 triatomic is distorted towards the $O+O_2$ configuration, the PES curvature and the bond length should change towards those of the diatomic O_2 product. This effect is incorporated into Eq. (5) by letting the Morse parameters r_e and a be coordinate-dependent quantities $r_e(r)$ and $a(r)$ in the form of shifted Gaussian functions. In the asymptotic channel region of our PES the equilibrium bond length obtained for O_2 product is 2.26 a.u. which is close to experimental value 2.28 a.u.[41] The asymptotic ZPE's obtained in the channels are 863.4 cm^{-1} for $^{16}O^{16}O$ product and 839.4 cm^{-1} for the $^{16}O^{18}O$ product, which gives us the correct $\Delta ZPE = 24.0$ cm^{-1} between the two channels.[18] Additional small corrections terms $V_{vdW}(r)$ are added to each channel in order to better reproduce the "tail" part of the ozone potential.[18] The last term $V_{inf}(r_1,r_2)$ in the form of a hyperbolic tangent function is used to fit the asymptotic value of the PES in the region of three body breakup (not considered in this paper). Experimental energy of 1.132±0.017 eV (Ref. 42) for dissociation $O_3 \rightarrow O+O_2$ is reproduced by the appropriate choice of parameters D_0 and D. Figure 1 gives a broad range view of our PES and a magnified view of its well region. Note that the general shape of this PES is typical for many barrierless recombination reactions.[43–45]

Our two-dimensional Hamiltonian is

$$H = \frac{p_1^2}{2\mu_1} + \frac{p_2^2}{2\mu_2} - \cos\theta_e \frac{p_1 p_2}{\mu_0} + V(r_1,r_2), \quad (6)$$

where $\theta_e=2.032$ is the bending angle frozen at its equilibrium value.[22] This approximation is justified by the fact that this angle changes only insignificantly along the minimum energy path for dissociation of O_3. The values of μ_1 and μ_2 represent the effective masses of diatomic products in two channels, while μ_0 is equal to the mass of the central atom.

The wave function is also two dimensional: $\psi(r_1,r_2) = \psi(\mathbf{r})$. In the IVR method,[31,32] the initial wave function $\psi(\mathbf{r},0)$ is expanded in terms of an overcomplete set of N Gaussian functions,

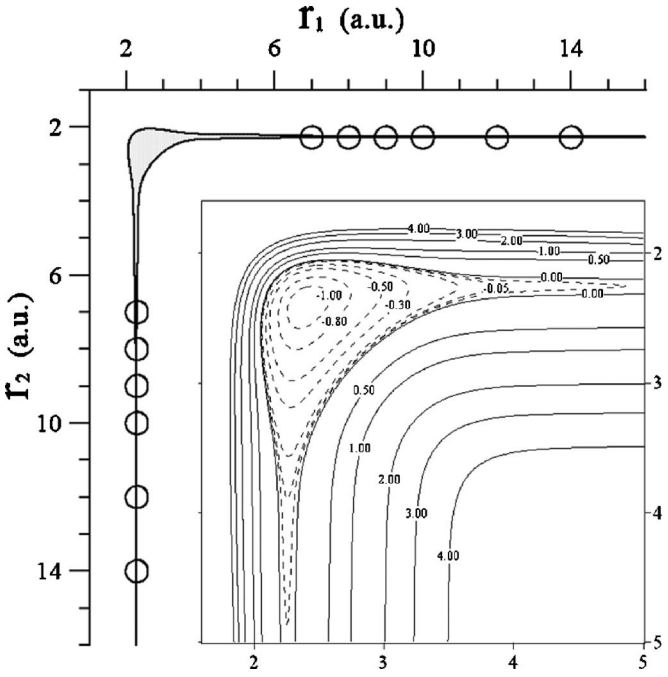

FIG. 1. Two views of the potential energy surface $V(r_1,r_2)$ used here to study recombination. The well depth is 1.13 eV. Energies of the contour lines are given in eV. Shaded area shows configuration space below the classical dissociation limit $E=0$. Circles represent the initial wave packets.

$$\psi_\gamma(\mathbf{r},\mathbf{r}_i,\mathbf{p}_i) \equiv \left(\frac{2\gamma}{\pi}\right)^{1/2} \exp\{-\gamma(\mathbf{r}-\mathbf{r}_i)^2 + i\mathbf{p}_i\cdot(\mathbf{r}-\mathbf{r}_i)\}. \tag{7}$$

These basis functions are placed randomly at various initial points $(\mathbf{r}_i,\mathbf{p}_i)$ in phase space and the time evolution of the wave function $\psi(\mathbf{r},t)$ is approximated by an integral over the initial phase space,

$$\psi(\mathbf{r},t) = \int \frac{d\mathbf{r}_i d\mathbf{p}_i}{(2\pi)^2} \langle \psi_\gamma(\mathbf{r},\mathbf{r}_i,\mathbf{p}_i)|\psi(\mathbf{r},0)\rangle_{\mathbf{r}} \times \psi_\gamma(\mathbf{r},\mathbf{r}_t,\mathbf{p}_t) C(\mathbf{r}_t,\mathbf{p}_t) e^{iS(\mathbf{r}_t,\mathbf{p}_t)}. \tag{8}$$

Each of N trajectories is propagated independently in the usual, classical way from its initial point $(\mathbf{r}_i,\mathbf{p}_i)$ to the final point $(\mathbf{r}_t,\mathbf{p}_t)$ at time t,

$$\dot{\mathbf{r}}_t = \frac{\partial H}{\partial \mathbf{p}}, \quad \dot{\mathbf{p}}_t = -\frac{\partial H}{\partial \mathbf{r}}. \tag{9}$$

All quantum mechanical effects are incorporated in Eq. (8) by calculating the classical action $S(\mathbf{r}_t,\mathbf{p}_t)$ and the preexponential factor $C(\mathbf{r}_t,\mathbf{p}_t)$ for each trajectory,[32]

$$C(\mathbf{r}_t,\mathbf{p}_t) = \left|\frac{1}{2}\left(\frac{\partial \mathbf{p}_t}{\partial \mathbf{p}_i} + \frac{\partial \mathbf{r}_t}{\partial \mathbf{r}_i} - 2i\gamma\frac{\partial \mathbf{r}_t}{\partial \mathbf{p}_i} + \frac{i}{2\gamma}\frac{\partial \mathbf{p}_t}{\partial \mathbf{r}_i}\right)\right|^{1/2}. \tag{10}$$

For simplicity, the initial wave packet $\psi(\mathbf{r},0)$ can be chosen as a Gaussian function characterized by the position $\mathbf{r}_0$, momentum $\mathbf{p}_0$, and the width parameter α,

$$\psi(\mathbf{r},0) = \psi_\alpha(\mathbf{r},\mathbf{r}_0,\mathbf{p}_0) \equiv \left(\frac{2\alpha}{\pi}\right)^{1/2} \exp\{-\alpha(\mathbf{r}-\mathbf{r}_0)^2 + i\mathbf{p}_0\cdot(\mathbf{r}-\mathbf{r}_0)\}. \tag{11}$$

In this case the overlap integral in Eq. (8) can be calculated analytically and the multidimensional integration in Eq. (8) can be carried out using a Monte Carlo scheme based on the Box-Müller algorithm.[32] Then, the final expression for the wave function is

$$\psi(\mathbf{r},t) = \frac{1}{N}\frac{2(\alpha+\gamma)}{\sqrt{\alpha\gamma}}\sum_{n=1}^{N} \psi_\gamma(\mathbf{r},\mathbf{r}_t,\mathbf{p}_t) \times C(\mathbf{r}_t,\mathbf{p}_t) e^{i(S(\mathbf{r}_t,\mathbf{p}_t)+\delta(\mathbf{r}_i,\mathbf{p}_i))}, \tag{12}$$

where we introduced

$$\delta(\mathbf{r}_i,\mathbf{p}_i) \equiv \frac{(\mathbf{r}_i-\mathbf{r}_0)\cdot(\alpha\mathbf{p}_i+\gamma\mathbf{p}_0)}{\alpha+\gamma}. \tag{13}$$

For analysis of the time-dependent wave packet we have to compute the autocorrelation function or the survival probability,

$$P(t) = \langle\psi(\mathbf{r},0)|\psi(\mathbf{r},t)\rangle_{\mathbf{r}}. \tag{14}$$

Using Eqs. (12) and (13) and calculating analytically the overlap integral in Eq. (14) we obtain

$$P(t) = \frac{4}{N}\sum_{n=1}^{N} C(\mathbf{r}_t,\mathbf{p}_t) e^{-A(\mathbf{r}_t,\mathbf{p}_t)+iB(\mathbf{r}_t,\mathbf{p}_t)}, \tag{15}$$

where we introduced

$$A(\mathbf{r}_t,\mathbf{p}_t) \equiv \frac{\alpha\gamma}{(\alpha+\gamma)}(\mathbf{r}_t-\mathbf{r}_0)^2 + \frac{1}{4(\alpha+\gamma)}(\mathbf{p}_t-\mathbf{p}_0)^2, \tag{16}$$

$$B(\mathbf{r}_t,\mathbf{p}_t) \equiv S(\mathbf{r}_t,\mathbf{p}_t) + \delta(\mathbf{r}_i,\mathbf{p}_i) - \delta(\mathbf{r}_t,\mathbf{p}_t). \tag{17}$$

Note that $P(t)$ in Eq. (15) is obtained as a sum over independent classical trajectories propagated numerically, which allows us to employ an efficient parallel algorithm for calculations of $P(t)$ using rather simple analytical expressions for $A(\mathbf{r}_t,\mathbf{p}_t)$, $B(\mathbf{r}_t,\mathbf{p}_t)$, and $C(\mathbf{r}_t,\mathbf{p}_t)$.

We found that the *bound* vibrational states localized in the well are very easy to characterize using the IVR propagation, because the spectrum is relatively sparse and also because many bound states can be captured simultaneously by a single Gaussian packet placed basically anywhere in the well. However, in order to give an accurate description of energies and lifetimes of the *metastable states* in the ΔZPE region and above, the parameters $(\mathbf{r}_0,\mathbf{p}_0)$ and α of the initial wave packet should be carefully chosen. This is because the spectrum of the scattering states is much denser, with many overlapping resonances. We found that in this situation the method works better if the initial wave packet covers only a narrow energy range and overlaps as much as possible with the wave function of one metastable state. Propagation of several such packets is required in order to cover the entire energy range of interest. We came out with the following recipe: In a barrierless potential the best position for the initial wave packet is far in the entrance or exit channel. This is

illustrated in Fig. 1, where we placed six wave packets along each channel with initial positions in the range $7<r_0<14$ a.u. This choice may look somewhat surprising but, as will be demonstrated below, it is justified by the shape of the wave functions for the scattering states. The width of the initial wave packet α should be comparable to the expected distance between the nodes of the wave functions in order to minimize cancellation of the overlap. Here we used $\alpha=50$. Finally, we found that the initial momentum should be set to zero. A nonzero momentum only increases quantum energy of the packet, broadens the energy window and shifts it up, away from the ΔZPE part of spectrum. Thus, we used $\mathbf{p}_0=0$ in Eqs. (11)–(17).

The major difficulty of the semiclassical IVR approach is associated with appearance of chaotic (unstable) trajectories.[36,38] For such trajectories the prefactor $C(\mathbf{r}_t,\mathbf{p}_t)$ becomes exponentially large, which leads to poor convergence of the method with respect to N and reduces accuracy of results. This is particularly the case for multidimensional potentials and at long propagation times, both specific to our system. Apparently, the problem was not that severe neither in the first study by Grossmann,[39] due to strongly repulsive PES and short propagation time, nor in our previous one-dimensional study,[29] where it could be overcome by increasing the number of trajectories, N. In this work, however, even with $N=10^7$ the propagation time was limited by the chaotic behavior to only $t\sim0.3-0.4$ ps, which is insufficient for spectral analysis. This behavior is seen very clearly in Fig. 2(a). To overcome this problem it was suggested by Kay[36] to monitor the values of $C(\mathbf{r}_t,\mathbf{p}_t)$ and remove any trajectory if its prefactor exceeds a chosen (large) cutoff value. Following this procedure we lost up to 15% of trajectories, which is highly undesirable at long propagation times when the sampling is already deteriorated by the wave packet spreading. Moreover, we observed that the long time behavior of $P(t)$ is rather sensitive to the choice of the cutoff value for the $|C(\mathbf{r}_t,\mathbf{p}_t)|$. We adopted a better approach. Since our primary purpose is to calculate the autocorrelation function $P(t)$ using Eq. (15) we should remove chaotic trajectories based only on the value of the product of the prefactor and the exponential factor for overlapping Gaussian functions: $|C(\mathbf{r}_t,\mathbf{p}_t)|e^{-A(\mathbf{r}_t,\mathbf{p}_t)}$. This new cutoff procedure allowed us to extend the propagation time by an order of magnitude keeping the amount of deleted trajectories at only 0.5%. The most important is that when the value of our cutoff parameter $|C(\mathbf{r}_t,\mathbf{p}_t)|e^{-A(\mathbf{r}_t,\mathbf{p}_t)}$ is varied in the working range (between 200.0 and 300.0) it has a negligible effect on the calculated autocorrelation function $P(t)$. Figure 2(a) gives an example of the autocorrelation function calculated using our cutoff procedure for a typical initial wave packet.

For comparison we propagated the same wave packet using the fully quantum Chebyshev method[46] and found that the quantum and semiclassical autocorrelation functions agree well during the initial 0.6 ps [see Fig. 2(b)]. Differences between the two methods at $t>0.6$ ps are due to errors of the quantum propagation, which requires a significant extension of the grid (due to fast motion of the wave packet into the channels) and becomes computationally impractical at ~1 ps. Note that the semiclassical method allows us to continue propagation to about 3.0–4.0 ps [see Fig. 2(a)] without an increase in the computational cost. In terms of the CPU time, the semiclassical IVR with $N=10^6$ was a factor of 25 faster compared to the quantum method. Another important feature of the IVR is its intrinsic massive parallelization. The N trajectories are totally independent and can be distributed among different processors and propagated in parallel without any message passing which gives a tremendous advantage in terms of the wall clock time. For example, we run our calculations using 1024 processors of the Seaborg machine at NERSC and achieved acceleration by another factor of 10^3 compared to one-processor quantum propagation.

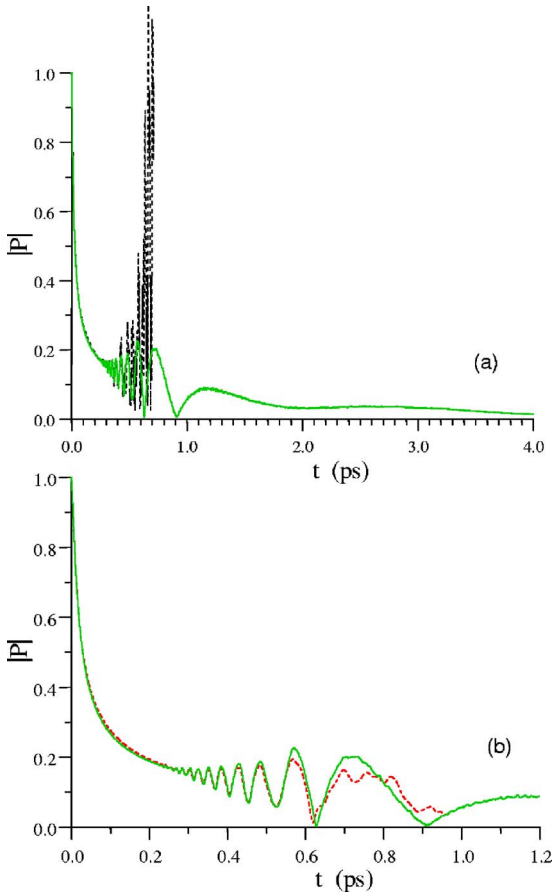

FIG. 2. (Color online): Autocorrelation functions obtained from propagations of a wave packet with initial coordinates $r_1=9.0$, $r_2=2.28$ a.u., and $\alpha=50$: (a) Semiclassical results calculated with all trajectories (black dashed) and with chaotic trajectories removed using new aproach (green solid). The standard propagation starts failing at about 0.3 ps and the advantage of the cutoff method is clearly seen. (b) Semiclassical (green solid) vs quantum (red dashed) results at shorter propagation times. See text for details.

III. ENERGIES, LIFETIMES, AND WAVE FUNCTIONS OF THE METASTABLE STATES

Figure 3 shows several examples of the half spectrum

$$I(E)=\left|\int_0^\infty P(t)e^{iEt}dt\right|^2 \tag{18}$$

calculated by numerical integration of the autocorrelation function $P(t)$ obtained from the IVR propagation, Eq. (15). As discussed in the previous section, the initial wave packets

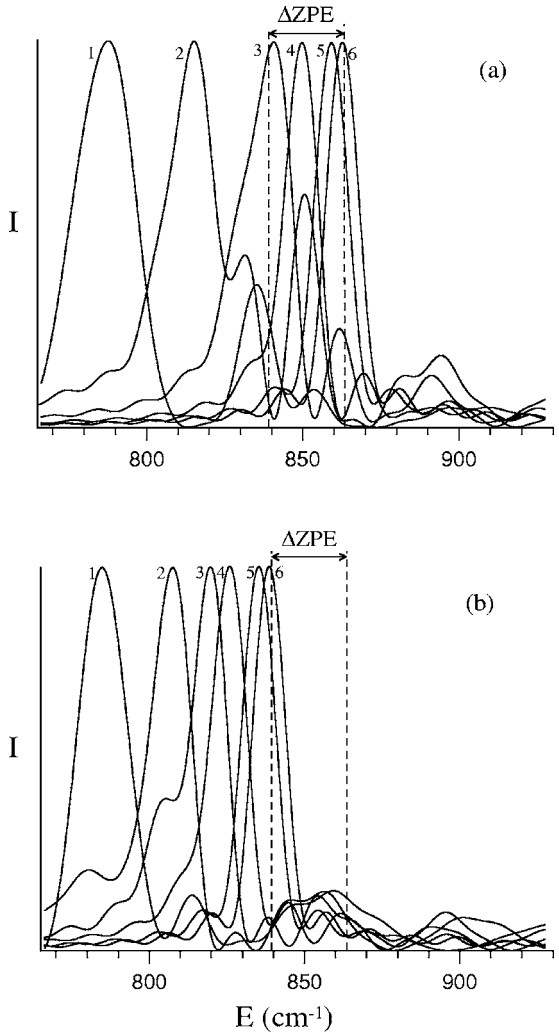

FIG. 3. Half spectra calculated from semiclassical propagation of the wave packets placed initially in (a) $^{16}O^{16}O+^{18}O$ and (b) $^{16}O+^{16}O^{18}O$ channels. Propagation time was $t=2.42$ ps, $N=10^7$, $\alpha=\gamma=50$. Initial positions for packets were $r_2^0=2.28$ a.u., $r_1^0=7.0$, 8.0, 9.0, 10.0, 12.0, and 14.0 a.u for lines 1–6 in frame (a); and $r_1^0=2.28$ a.u., $r_2^0=7.0$, 8.0, 9.0, 10.0, 12.0, and 14.0 a.u. for lines 1–6 in frame (b).

are placed far into the channels of the PES where they overlap significantly with only one state. As a result, all the spectra in Fig. 3 exhibit only one or two pronounced narrower peaks and several less definite broader peaks (typically 10 or more) with gradually decreasing amplitude. It is well known that if the resonances are isolated, $\Gamma_j/2 \ll (E_j - E_{j-1})$, the integration in Eq. (18) can be carried out analytically and the half spectrum can be approximated by[29]

$$I(E) \approx \sum_{j=1}^{L} |b_j|^4 \frac{1}{(\Gamma_j/2)^2 + (E-E_j)^2}, \tag{19}$$

where b_j are the probability amplitudes of different states in the initial wave packet. Equation (19) indicates that the half spectrum should exhibit a set of Lorentzian peaks showing positions and widths of the metastable states. Figure 3 shows very clearly that at energies *above* the ΔZPE range all the peaks are relatively broad regardless of into which channel the initial wave packet was placed. [Note that Figs. 3(a) and 3(b) contain the results obtained by placing the initial wave packets into the channels $^{16}O^{16}O$ and $^{16}O^{18}O$, respectively.] The situation *within* the ΔZPE range is qualitatively different. Here the wave packets placed into the $^{16}O^{18}O$ channel still produce broader peaks, while the wave packets placed into the $^{16}O^{16}O$ channel produce much narrower peaks, similar to those found at energies *below* the ΔZPE where all the quantum states are stable (bound). Thus, the half spectra of Fig. 3 indicate the existence of metastable states of two types. All the metastable states above the ΔZPE exhibit short lifetimes; they significantly overlap each other and gradually transform into a continuous spectrum. However, the resonances within the ΔZPE range can be either short or long lived. Apparently, this depends on the channel.

Figure 3 also demonstrates that, due to the finite propagation time and high density of states, the majority of peaks do not represent isolated Lorentzians. Thus, it is not really appropriate to try fitting the half spectrum $I(E)$ with Eq. (19). The values of E_j and Γ_j obtained this way will be very inaccurate and highly sensitive to the propagation time. A much better approach is to extract E_j and Γ_j directly from $P(t)$ using the Prony method[47] where the autocorrelation function, calculated on a grid of time points, is fitted by

$$P(t) = \sum_{j=1}^{L} b_j \exp\{-i(E_j - i\Gamma_j/2)t\}, \tag{20}$$

and the unknown coefficients b_j, E_j, and Γ_j are determined using a nonlinear least-squares method. The value of L is also unknown but can be determined by trial and error. The restriction is $L \leqslant M/2$, where M is the number of points in the autocorrelation function.[47] The disadvantage of this method is related to occurrence of false resonances and some uncertainty in the error bars for each resonance. (Precision of the fit of the entire spectrum is not really useful.)

We found it helpful to combine both methods and use $I(E)$ for preliminary analysis of the entire spectrum of the wave packet, followed by the Prony analysis focused on narrow energy range. The results are given in Table I, where the spectrum is divided onto two columns according to the channel where the initial wave packet was placed, either $^{16}O^{16}O$ or $^{16}O^{18}O$. Each autocorrelation function was analyzed several times using different L and M and the precision of each E_j and Γ_j value was estimated as its deviation from an average value when L and M are varied. The precision of E_j values for upper bound states (just below the ΔZPE range) is about 0.2 cm^{-1}. For the scattering states in the ΔZPE region it is about 0.4 cm^{-1} and grows up to 1.0 cm^{-1} for the states near the 900 cm^{-1} (see Table I), which is very good. The precision of widths for all broader resonances is about 10% of Γ_j values that is from 1.5 up to 30.0 cm^{-1}, which is quite satisfactory. This includes all the states in the $^{16}O^{18}O$ channel and the states in the $^{16}O^{16}O$ channel at energies above the ΔZPE. Within the ΔZPE region in the $^{16}O^{16}O$ channel the resonances are extremely narrow so that accurate determination of their widths was not straightforward. For these resonances the Prony analysis showed that their widths belong to the range $\Gamma_j < 1.0$ cm^{-1} (which corresponds to lifetimes $\tau > 50$ ps) but the actual values were very unstable with respect to L which resulted in the error bars of the same order

TABLE I. Energies and widths of bound and metastable states of $^{16}O^{16}O^{18}O$ in the vicinity of the ΔZPE energy range using 2D potential from Eq. (1). These data were obtained via Prony analysis of autocorrelation functions calculated using semiclassical propagation of wave packets shown in Fig. 1.

	Closed channel, $^{16}O^{16}O$		Open Channel, $^{16}O^{18}O$	
	$E(cm^{-1})$	$\Gamma(cm^{-1})$	$E(cm^{-1})$	$\Gamma(cm^{-1})$
Metastable states above the ZPE of $^{16}O^{16}O$	...		...	
			899.3	325.0
	894.5	101.0		
	891.3[a]	58.0	891.2[a]	55.0
			885.6	135.0
	881.6	42.0		
	875.1	27.0		
			872.7	100.0
	865.5	16.0		
			865.4	66.0
Metastable states within the ΔZPE region	861.4	0.06±0.03		
			861.4	40.0
	858.2	0.06±0.04		
			857.4	36.0
	850.9	0.06±0.04		
			845.3	26.5
			841.2	15.0
	840.4	0.06±0.05		
Bound states below the ZPE of $^{16}O^{18}O$			837.2	
	835.6			
			825.8	
	817.0			
			807.3	
	788.0			
			784.7	
	...		...	

[a]A symmetric stretch state.

of magnitude, ±1.0 cm^{-1}. Simply increasing the propagation time did not help, which makes us to believe that this problem is due to the noise that appears in the semiclassical autocorrelation functions at $t>0.8$ ps, as can be seen in Fig. 2. This noise is probably due to removal of chaotic trajectories. The important role of such trajectories has been noted in Refs. 36 and 38.

We found three ways to improve precision of Γ values for such narrow resonances in the ΔZPE region. First, we increased the number of trajectories to $N=10^8$. Second, we applied smoothing to the noisy autocorrelation function prior to running its Prony analysis. Finally, we used eigenfunction $\phi_j(r)$ obtained from the first IVR propagation (see below) as a refined initial wave packet $\psi(\mathbf{r},0)$ for an additional second propagation. This last method produces a noise-free very simple looking autocorrelation function (with the dominant amplitude b_j close to one) and improves accuracy dramatically. The disadvantages are inability to use the Box-Müller algorithm for sampling and the increase of the computational cost. Using this approach for narrow resonances in the ΔZPE region we obtained $\Gamma_j \approx 0.06$ cm^{-1} with the error bars given in Table I. We observed better precision for those states that are more isolated. For example, from Fig. 3(a) (curve 3) we see that the state at $E=840.4$ cm^{-1} significantly overlaps the state at $E=835.6$ cm^{-1}, which leads to somewhat lower accuracy. On the other hand, the state at $E=861.4$ cm^{-1} (curve 6 on the same figure) is completely isolated in the half spectrum, which results in a slightly better precision for its value of Γ.

The data given in Table I for widths of the scattering resonances support our observation of the unusual relationship between the lifetimes and the channels. Further insight is obtained from analysis of their wave functions.

When energies E_j are known, the wave functions of the metastable states can be found from the Fourier transform of the propagated wave packets,

$$\phi_j(\mathbf{r}) \approx \int_0^\infty \psi(\mathbf{r},t) e^{iE_j t} dt. \tag{21}$$

Typical examples are given in Figs. 4 and 5. Figure 4 shows the wave functions for two very narrow resonances in the ΔZPE range. Imaginary parts of these wave functions are very small, which is consistent with small values of the corresponding Γ_j's given in Table I. The striking feature of these states is their almost perfect localization along the $^{16}O^{16}O$ channel with maximum probability points found far in the channel at $r_1 \sim 9.0$ and 11.0 a.u., respectively. Note that at energies within the ΔZPE range this channel is still closed for decay of the metastable O_3^* states and, although such

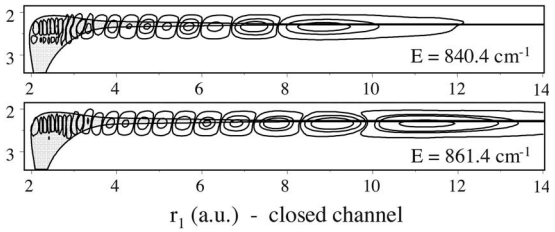

FIG. 4. Modulus of the wave functions for two metastable states at $E=840.4$ and 861.4 cm^{-1} obtained from semiclassical propagation of a Gaussian wave packet with $\alpha=50$, $r_1=9.0$, and $r_2=2.28$ a.u. The wave functions are entirely localized in the closed channel and the lifetimes are very large.

states are energetically metastable, the only pathway available for their decay is through the other channel of the PES, which describes $^{16}O^{18}O$ products and (due to lower ZPE) is already open at these energies. One can probably say that although these states are energetically unstable, they are topologically trapped. But the trapping is not by a barrier of any sort. In order to decay these states do not need to tunnel, the open channel is around the corner (see Fig. 1), but they have to "flow" through the well region of the PES. Put another way, the molecular geometry and the internal energy distribution would have to rearrange from the $^{16}O^{16}O-^{18}O$-like into the $^{16}O-^{16}O^{18}O$-like. As a result these states exhibit anomalously long lifetimes, $\tau\sim 100$ ps. One can also say that these states are trapped by quantum ZPE. To the best of our knowledge resonances of this type have never been described in the literature before and is one of the

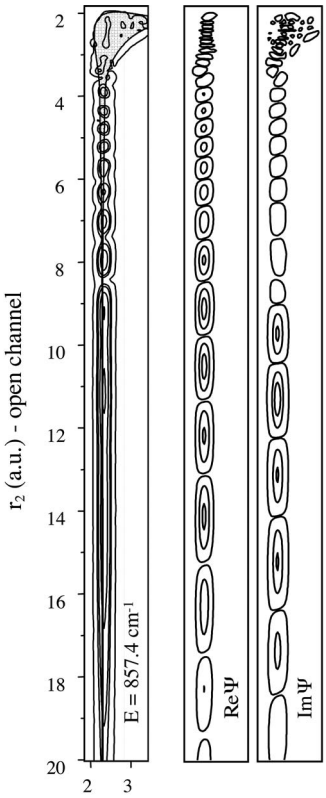

FIG. 5. Modulus, real, and imaginary parts of the wave function for the metastable state at $E=857.4$ cm^{-1} obtained from semiclassical propagation of a Gaussian wave packet with $\alpha=50$, $r_1=2.28$, and $r_2=9.0$ a.u. The wave function is entirely localized in the open channel and the lifetime is short.

major findings of this paper. All the narrow resonances in the ΔZPE range exhibit this property and we believe it is general and may occur in other molecules as well. Also, there is some similarity in the nature of these long-lived metastable states and the true bound states of heavy-light-heavy systems such as I+HI, where the bound states are formed in the absence of any attractive well due to vibrationally adiabatic stabilization of the transition state region of a repulsive PES.[48–50]

Figure 5 represents wave function for a typical broad metastable state in the ΔZPE range. Since the width Γ_j for this state is significant, the imaginary part of the wave function is comparable to its real part and both are given in Fig. 5. The real and imaginary parts oscillate with gradually decreasing amplitudes up to $r_2\sim 20.0$ a.u., while the modulus of the wave function oscillates up to $r_2\sim 9.0$ a.u. where it reaches the maximum value and then exhibits a very long tail. This wave function is also entirely localized in one channel, but this channel corresponds to the $^{16}O^{18}O$ product and is open. Opposite to the cases shown in Fig. 4, the decay of this state through the open channel is direct and much faster, which is reflected by its short lifetime $\tau\approx 0.15$ ps. We found that wave functions of all broad resonances in the ΔZPE region look qualitatively similar to the example given in Fig. 5. Note that the difference of energies of the states presented in Figs. 4 and 5 is quite small (only 4 cm^{-1}) while their lifetimes differ by three orders of magnitude. The reason for this unusual behavior is now clear. It is due to localization of the wave functions in only one channel which can be either closed or open (due to ΔZPE).

Also, Figs. 4 and 5 explain why the scattering states are captured well only by the wave packets started far in the channels. The intensity of peaks in the half spectrum is proportional to the amplitudes b_j in Eq. (19). These amplitudes represent the value of the overlap between the initial wave packet and the wave function for a given state. Since wave functions for the scattering states exhibit maxima far in the channels, the initial wave packets placed in those regions will be most efficient. On the contrary, wave packets started in the well region contain a large number of bound states so that the scattering states they contain are much harder to resolve.

As an additional test of the IVR calculations and in order to understand why the wave functions of the scattering states are localized in only one channel, we decided to calculate and inspect the wave functions of the bound states. The Hamiltonian matrix was diagonalized in the basis of 95×95 harmonic oscillator functions using our 2D potential from Fig. 1. For the $^{16}O^{16}O^{18}O$ isotopomer we found more than 70 states below the dissociation limit. For the majority of these states, the difference between the eigenvalues obtained by diagonalization (quantum) and Prony analysis of wave packets (semiclassical) was about 0.2 cm^{-1}. As usual, the wave functions of the vibrational states near the bottom of the well can be assigned introducing two quantum numbers ν_{sym} and ν_{asym} for progressions of symmetric (r_1+r_2) and antisymmetric (r_1-r_2) stretch normal modes, respectively. Even for an asymmetric ozone isotopomer $^{16}O^{16}O^{18}O$ all such wave functions look quite symmetric and each of

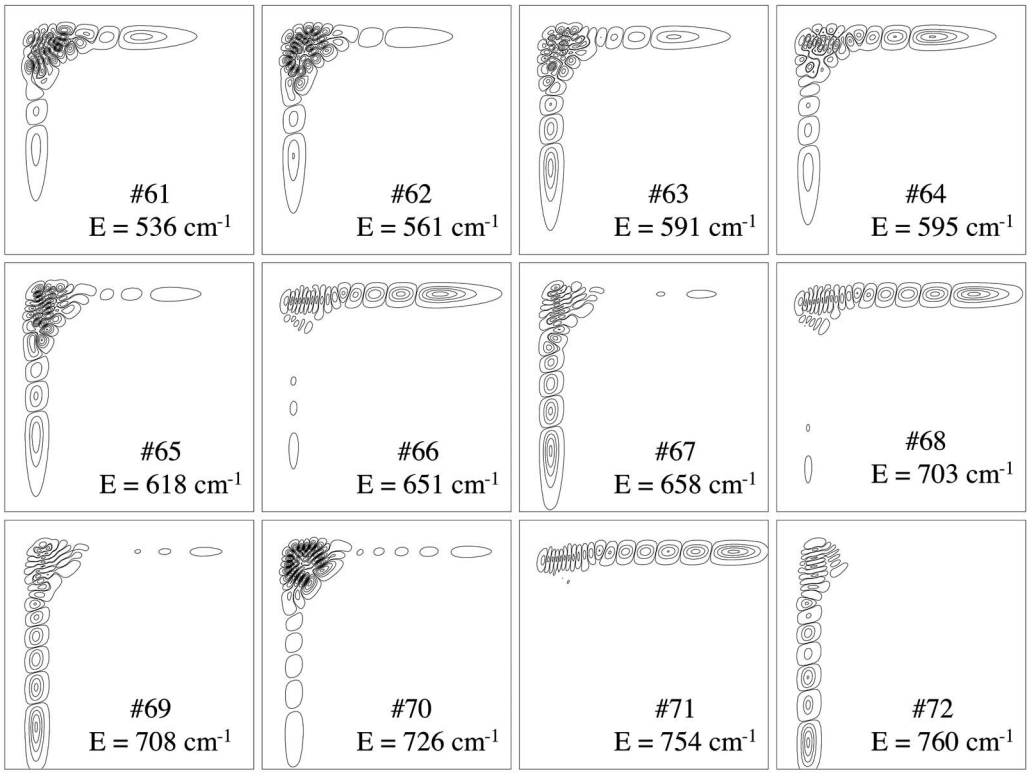

FIG. 6. Eigenfuctions (obtained from diagonalization) for the bound states in the range from 536 to 760 cm^{-1}. Transformation of the normal mode character into the local mode character is clearly seen. States are numbered starting at the ground vibrational state.

them exhibits about equal probability in two channels. However, starting as early as $\nu_{asym}=2-3$, the progression of antisymmetric stretch normal mode states transforms into two independent progressions of the *local vibration mode* states localized in the corresponding channels and characterized by new quantum numbers $\nu_{16-1618}$ and $\nu_{1616-18}$. The wave functions from the energy region where this transformation takes place (536–760 cm^{-1}) are given in Fig. 6. Readers can see that several lower states here, 61–64, are still quite symmetric. Staring at state 65 the localization in the channels becomes very pronounced and continues to develop as vibrational excitation increases. The last two states here, 71 and 72, are already entirely local and are qualitatively similar to the metastable states given in Figs. 4 and 5. A similar effect of transition from the normal mode character to a very pronounced local mode character has been observed earlier in the bound state spectra calculated for SO_2 molecule.[51]

Note that the progression of the symmetric stretch normal mode states survives and such wave functions spread about equally over the two channels. However, since one quantum of the symmetric stretch is very large (compared to one quantum of the local stretch) the spacing between these states is also very large and such states are rare. The last bound state of this kind is found at $E=726.7$ cm^{-1} and is 70 in Fig. 4. The next symmetric state is a metastable state at 891 cm^{-1} marked by superscript (a) in Table I. Note that this state is already above the ΔZPE range. Because its wave function is about symmetric, it is captured by the initial wave packet started in any channel and this is reflected in Table I. The value of the width for this symmetric state is intermediate between the widths of states in the open and closed channels.

IV. KINETICS

As outlined in the introduction we consider the energy transfer mechanism of ozone formation, Eqs. (2) and (3), and assume that every metastable state is in equilibrium with reactants/products. To simplify notations we introduce the label A for the $^{16}O^{18}O$ channel (open at energies within the ΔZPE range due to lower ZPE) and the label B for the $^{16}O^{16}O$ channel (closed at these energies due to higher ZPE). As we demonstrated in the previous section, the majority of metastable states are localized in only one channel. Formation and decay of such localized states will occur most efficiently through this channel and in most cases we can neglect contribution from another channel. This approximation is applicable to all the metastable states of channel A (shown as dashed blue lines in the diagram of Fig. 7),

$$^{A}O + {}^{A}O_2 \rightleftarrows {}^{A}O_3^*(E_j), \quad E_j > {}^{A}\mathrm{ZPE}, \tag{22}$$

and to the metastable states of channel B with energies above the ^{B}ZPE (shown as dashed green lines in Fig. 7),

$$^{B}O + {}^{B}O_2 \rightleftarrows {}^{B}O_3^*(E_j), \quad E_j > {}^{B}\mathrm{ZPE}. \tag{23}$$

An important exception should be made for those narrow metastable states within the ΔZPE energy range. Although perfectly localized in channel B, they cannot be populated from this channel because this channel is still closed at these collision energies. Thus, for such states the contribution of channel A is the only one available and must be taken into account (shown as dotted red lines in Fig. 7),

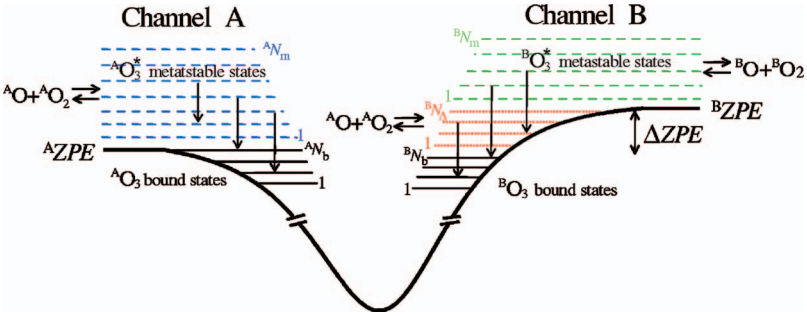

FIG. 7. (Color) Formation process of an asymmetric ozone isotopomer through two entrance channels different by the ΔZPE. Solid and dashed lines represent bound and metastable states, respectively. See text and Appendix for discussion.

$$^{A}\mathrm{O}+{}^{A}\mathrm{O}_2 \rightleftarrows {}^{\Delta}\mathrm{O}_3^*(E_j), \quad {}^{A}\mathrm{ZPE} < E_j < {}^{B}\mathrm{ZPE}. \tag{24}$$

The second exception is made for those rare symmetric stretch states spread over both channels. In such cases the contributions of the two channels is assumed to be 50/50,

$$^{A}\mathrm{O}+{}^{A}\mathrm{O}_2 \rightleftarrows {}^{\mathrm{SYM}}\mathrm{O}_3^*(E_j) \rightleftarrows {}^{B}\mathrm{O}+{}^{B}\mathrm{O}_2, \quad E_j > {}^{B}\mathrm{ZPE}. \tag{25}$$

These rare states are not shown in Fig. 7 for simplicity. Note that in formula (22)–(25) the superscripts A and B are used in order to relate to one or the other channel (i) the metastable O_3^* states, (ii) the atomic and diatomic reactants and products, and (iii) the ZPEs.

To characterize the processes of formation and decay of the metastable states we introduce for every state the rate constants k_j^f and k_j^d, respectively. Decay is a first order kinetic process and its rate is simply related to the width of the state,

$$k_j^d = \Gamma_j. \tag{26}$$

The formation rate constant k_j^f is then found from the detailed balance as $k_j^f = K_j k_j^d$, where the equilibrium constant is calculated in a standard way using statistical mechanics. For example, for the states populated from channel A,[52]

$$^{A}K_j = \left(\frac{2\pi}{{}^{A}\mu kT}\right)^{3/2} \exp\left\{-\frac{E_j - {}^{A}\mathrm{ZPE}}{kT}\right\}. \tag{27}$$

The expression for $^{B}K_j$ is similar to Eq. (27) but contains the reduced mass $^{B}\mu$ and ^{B}ZPE of the channel B. For the stabilization rate constant k_{ji}^s we adopted the "exponential down" model,[15,19,25] where for a transition from the metastable state at energy E_j to another metastable or stable state at energy E_i the stabilization rate decreases exponentially with the increase of the energy gap,

$$k_{ji}^s = \omega(T)\exp\left\{-\frac{E_j - E_i}{\Delta E}\right\}. \tag{28}$$

Here $\omega(T)$ is the temperature dependent Lennard-Jones collision frequency for O_3^*+M stabilizing collisions,[15,19,25] and $\Delta E = 20\ \mathrm{cm}^{-1}$ is the experimental value for ozone.[53] Note that for the metastable states localized in one channel it is enough to consider only the stabilizing transitions onto the states of the same channel, either A-to-A or B-to-B transitions, that is, the transitions within the same local vibration mode progression, either within $\nu_{16-1618}$ or within $\nu_{1616-18}$. This is justified by the fact that the overlap between the states localized in different channels is very small (imagine overlapping Figs. 4 and 5) and the probability of such A-to-B or B-to-A transitions must be negligibly small.

Derivation of the expressions for the channel specific third order reaction rate coefficients of ozone formation, $^{A}\kappa$ and $^{B}\kappa$, is given in the Appendix. It is based on preequilibrium approximation and uses Eqs. (3) and (22)–(28). The final and most general result is given by Eqs. (A10)–(A16). Using the values of E_j and Γ_j for all states from Table I, the values of $^{A}\kappa$ and $^{B}\kappa$ can be calculated and the resultant isotope effect $R = {}^{B}\kappa/{}^{A}\kappa$ can be predicted. But first we discuss two limiting cases when the complicated expressions (A10)–(A16) become most transparent.

We showed earlier[29] that within the framework of a three-state model formulated for a single-channel problem there are two limiting cases when the actual values of Γ_j's for the metastable states become unimportant for the kinetics, so that the reaction rate coefficient κ is entirely determined by the values of E_j's. Namely, in the limit of broad (short-lived) resonances, $\Gamma_j \gg k_{ji}^s[M]$, the rate coefficient κ depends only on energy gap between the states, $E_j - E_i$. In the opposite limit, $\Gamma_j \ll k_{ji}^s[M]$, the narrow (long-lived) resonances can be treated simply as stable states.[29] In the Appendix to this paper we show that similar limiting cases can be formulated for the multistate two-channel problem studied here. The values of Γ_j should satisfy generalized conditions (A17) and (A19), respectively. First we focus on the limit when all the resonances are broad and the reaction rate coefficients for two channels can be calculated as (see Appendix)

$$^{A}\kappa \approx \sum_{j=1}^{{}^{A}N_m}\sum_{i=1}^{{}^{A}N_b} {}^{A}K_j k_{ji}^s + \sum_{j=1}^{{}^{B}N_\Delta}\sum_{i=1}^{{}^{B}N_b} {}^{A}K_j k_{ji}^s, \tag{29}$$

$$^{B}\kappa \approx \sum_{j=1}^{{}^{B}N_m}\sum_{i=1}^{{}^{B}N_b} {}^{B}K_j k_{ji}^s. \tag{30}$$

Here the first term in each expression describes contribution from stabilization of the metastable states at energies above the ZPE in each channel (labeled by j from 1 to either $^{A}N_m$ or $^{B}N_m$) onto the bound states of the same channel (labeled by i from 1 to either $^{A}N_b$ or $^{B}N_b$). In Fig. 7 these processes are shown as blue-to-black and green-to-black transitions. The second term in Eq. (29) describes the contribution from stabilization of the metastable states in the ΔZPE energy range in channel B (labeled by j from 1 to $^{B}N_\Delta$) onto the bound states of the same channel. In Fig. 7 these processes are shown as red-to-black transitions. Note that although these states belong to channel B they contribute to $^{A}\kappa$ because they

are populated only through channel A due to ΔZPE (see Fig. 7). This effect leads to a significant increase of ${}^{A}\kappa$ relative to ${}^{B}\kappa$ and appearance of the anomalous isotope effect. In the limit of broad resonances this effect is most significant; using Eqs. (29) and (30) and energies E_j from Table I we obtain $R={}^{B}\kappa/{}^{A}\kappa\approx 0.14$. Analysis of Eq. (A17) shows that this limiting case would be reached if all states would have $\Gamma_j > 0.4$ cm^{-1}. From Table I we see that all metastable states in channel A and the states above ^{B}ZPE in channel B are broad enough. However, the values of Γ_j for narrow resonances in the closed channel are too small to satisfy this condition. Thus, the limit of broad resonances is not reached in our case and the isotope effect should not be that significant. Still, we want to emphasize that Eq. (29) is a very important result of the paper. It shows very clearly that the anomalous isotope effect is due to the second additional term in Eq. (29) which describes contribution of the metastable states in the ΔZPE energy range and leads to $R<1.0$.

It is also instructive to consider another limiting case, when the resonances in the ΔZPE range in channel B are very narrow, as in Eq. (A19), while all other resonances (as was assumed in the previous example and is indeed the case) are again broad. It is shown in the Appendix that in this case the population and stabilization of the metastable states in each channel occurs independently from another channel and the reaction rate coefficients for two channels are simply

$$ {}^{A}\kappa \approx \sum_{j=1}^{{}^{A}N_m} \sum_{i=1}^{{}^{A}N_b} {}^{A}K_j k_{ji}^{s}, \tag{31} $$

$$ {}^{B}\kappa \approx \sum_{j=1}^{{}^{B}N_m} \sum_{i=1}^{{}^{B}N_b} {}^{B}K_j k_{ji}^{s} + \sum_{j=1}^{{}^{B}N_m} \sum_{j'=1}^{{}^{B}N_\Delta} {}^{B}K_j k_{jj'}^{s}, \tag{32} $$

Note that in Eq. (32) for channel B the metastable states above ^{B}ZPE are stabilized onto the narrow metastable states in the ΔZPE range, i.e., the long-lived resonances play the role of the bound states. The anomalous isotope effect disappears in this case [compare to Eqs. (29) and (30)] and the difference between ${}^{A}\kappa$ and ${}^{B}\kappa$ can only be due to the number of states and the energy gaps between them, i.e., due to the different density of states in channels A and B. One would call this a normal isotope effect. Since $\mu_{16+1618}=10.78$ and $\mu_{1616+18}=11.52$ (i.e., ${}^{A}\mu < {}^{B}\mu$) we should expect $R>1$. Indeed, using energies E_j from Table I in Eqs. (31) and (32) we obtain $R=1.30$. Analysis of Eq. (A15) shows that this limit is reached only when $\Gamma_j < 0.003$ cm^{-1} ($\tau > 2$ ns), which means that our narrow resonances are not narrow enough for this limit and the anomalous isotope effect in our case should not disappear in favor of the normal isotope effect.

Thus, the actual values of widths of the narrow resonances in the ΔZPE part of spectrum appear to be crucial for accurate prediction of the isotope effect. Using the general formula (A10)–(A16) and the actual data from Table I we obtain $R=0.36-0.72$, where uncertainty is due to the error bars of Γ_j values of narrow resonances (see Table I). Note that experimental value of $R_{\mathrm{exp}}\approx 0.63$ for $^{16}O^{16}O^{18}O$ falls in this range. However, we should admit that the uncertainty is quite large. It is thus an important conclusion of this work that the isotope effect is very sensitive to the values of Γ_j for those narrow resonances in the ΔZPE range.

V. CONCLUSIONS

In this paper we report two important developments. First, we show that the semiclassical IVR method can be successfully applied to calculate energies, lifetimes, and wave functions of long-lived scattering resonances (metastable states) in a barrierless potential with a deep attractive well and long range interaction tails in the channels. Using a new cutoff procedure for chaotic trajectories, we achieved stable propagation of wave packets for up to $t=4.0$ ps. The number of trajectories needed to obtain converged results was, as usual, large ($N=10^6-10^8$ at $t=0$) but, since the trajectories are totally independent, the parallel processing was also very efficient. The intrinsic massive parallelization of the method allowed us to achieve the wall-clock-time acceleration by several orders of magnitude. This demonstrates that the IVR approach to scattering resonances is computationally appealing. The results of semiclassical wave packet propagation agreed well with fully quantum results. Autocorrelation functions were computed and then analyzed using the Prony method which permits one to extract energies and widths of the resonances. Further improvement of accuracy for widths of very narrow resonances seems to be possible by employing a method of analysis (other then Prony) that would be less sensitive to the noise present in the semiclassical autocorrelation function at long propagation times.

Second, we use this approach to study recombination reaction which forms an asymmetric ozone isotopomer $^{16}O^{16}O^{18}O$. We demonstrate that wave functions of the metastable O_3^* states are highly localized in one or another channel. This interesting behavior can be explained by introducing two independent progressions of highly excited vibrational states for $^{16}O^{16}O-{}^{18}O$ and $^{16}O-{}^{16}O^{18}O$ local stretch modes. We show that within the ΔZPE energy range, when the $^{16}O^{16}O$ channel is still energetically closed, the metastable states of the $^{16}O^{16}O-{}^{18}O$ progression are very long lived ($\tau\sim 50-500$ ps) while the states of the $^{16}O-{}^{16}O^{18}O$ progression decay much faster ($\tau\sim 0.1-0.3$ ps). This property correlates with the local mode character found in the wave functions. The nature of such narrow resonances in the ΔZPE energy range is somewhat similar to the Feshbach resonances which occur due to interaction between open and closed electronic channels. The difference is that in our case only one electronic state is involved and the two channels are the $^{16}O^{16}O+{}^{18}O$ and the $^{16}O+{}^{16}O^{18}O$ channels of a chemical reaction. The two channels are coupled by the PES, one is open and one is closed due to quantum ΔZPE.

Finally, we study kinetics of this reaction and show that these long-lived resonances in the ΔZPE energy range are responsible for the anomalous isotope effect found in ozone. We demonstrate that the isotope effect is extremely sensitive to lifetimes of these states. Thus, accurate determination of widths of narrow resonances (in the range between 0.4 and 0.003 cm^{-1}) becomes crucial for correct prediction of the isotope effect.

In this work we consider a simplified 2D model of ozone formation where the angle θ in the Hamiltonian of Eq. (6) was fixed. This is certainly an approximation, though it is justified by the fact that the contribution of the insertion reactions of type ${}^{Y}O+{}^{X}O^{Z}O \rightarrow {}^{X}O^{Y}O^{Z}O$ is known to be very small in ozone. Of course, for the accurate prediction of the isotope effect an extension of this work onto a three-dimensional problem with a full dimensional accurate PES is necessary. Using the semiclassical IVR approach and the methodology developed here such an extension should be relatively straightforward and we plan to explore this opportunity in the future.

ACKNOWLEDGMENTS

This research was partially supported by the Petroleum Research Fund, Grant No. 43298-G6. It also used resources of the National Energy Research Scientific Computing Center, supported by the Office of Science of the U.S. Department of Energy under Contract No. DE-AC03-76SF00098.

APPENDIX: CHANNEL SPECIFIC RECOMBINATION RATE COEFFICIENT

The process of formation of an asymmetric ozone isotopomer (such as ${}^{16}O^{16}O^{18}O$, for example) is represented in Fig. 7. Two entrance channels and the well region are shown. All the stable and metastable O_3^* states important for the recombination process are shown schematically. States are divided into groups according to their role; color is used to simplify understanding. All the states are numbered from going up from the bottom. In channel A the two groups of states are bound states ${}^{A}O_3(E_i)$ below the ^{A}ZPE, labeled by $1 \leqslant i \leqslant {}^{A}N_b$ (solid black) and metastable states ${}^{A}O_3^*(E_j)$ above the ^{A}ZPE, labeled by $1 \leqslant j \leqslant {}^{A}N_m$ (dashed blue).

In channel B there are three groups of states: bound states ${}^{B}O_3(E_i)$ below the ^{A}ZPE, labeled by $1 \leqslant i \leqslant {}^{B}N_b$ (solid black), metastable states ${}^{\Delta}O_3^*(E_j)$ below the ^{B}ZPE, labeled by $1 \leqslant j \leqslant {}^{B}N_\Delta$ (dotted red), and metastable states ${}^{B}O_3^*(E_j)$ above the ^{B}ZPE, labeled by $1 \leqslant j \leqslant {}^{B}N_m$ (dashed green).

Note that subscript Δ is used to number the narrow metastable states within the ΔZPE part of spectrum. Subscript m is used for all other metastable states. Subscript b is used for the bound states. Thus, only the value of ${}^{B}N_\Delta$ is strictly defined, while the values of ${}^{A}N_b$, ${}^{A}N_m$, ${}^{B}N_b$, and ${}^{B}N_m$ are somewhat arbitrary because we should only consider upper bound and lower metastable states in the vicinity of the reaction threshold (but we should include enough of them, of course). The symmetric stretch states (rare due to large quantum of the vibrational energy for this mode) are not shown in this picture for simplicity.

The rate of ozone formation can be obtained by looking at the buildup of concentrations of stable O_3 states (labeled by i) due to stabilization of the metastable O_3^* states (labeled by j),

$$\text{rate} = \sum_{i=1}^{{}^{A}N_b} \left(\frac{d[{}^{A}O_3(E_i)]}{dt} \right) + \sum_{i=1}^{{}^{B}N_b} \left(\frac{d[{}^{B}O_3(E_i)]}{dt} \right), \tag{A1}$$

where for every bound state we can write

$$\frac{d[{}^{A}O_3(E_i)]}{dt} = \sum_{j=1}^{{}^{A}N_m} k_{ji}^{s}[{}^{A}O_3^*(E_j)][\mathrm{M}], \quad 1 \leqslant i \leqslant {}^{A}N_b \tag{A2}$$

$$\frac{d[{}^{B}O_3(E_i)]}{dt} = \sum_{j=1}^{{}^{B}N_m} k_{ji}^{s}[{}^{B}O_3^*(E_j)][\mathrm{M}] + \sum_{j=1}^{{}^{B}N_\Delta} k_{ji}^{s}[{}^{\Delta}O_3^*(E_j)][\mathrm{M}], \quad 1 \leqslant i \leqslant {}^{B}N_b. \tag{A3}$$

Here [M] is the concentration of the bath gas molecules. The second-order stabilization rate constant k_{ji}^{s} for stabilizing transition $E_j \rightarrow E_i$ can be calculated using Eq. (28). Concentrations of the metastable states for each channel ($[{}^{A}O_3^*(E_j)]$, $[{}^{\Delta}O_3^*(E_j)]$, and $[{}^{B}O_3^*(E_j)]$) are needed here and can be found as follows. For each metastable state in channel A the master equation is

$$\frac{d[{}^{A}O_3^*(E_j)]}{dt} = k_j^{f}[{}^{A}O][{}^{A}O_2] - k_j^{d}[{}^{A}O_3^*(E_j)] - \sum_{i=1}^{{}^{A}N_b} k_{ji}^{s}[{}^{A}O_3^*(E_j)][\mathrm{M}] - \sum_{j'=1}^{j-1} k_{jj'}^{s}[{}^{A}O_3^*(E_j)][\mathrm{M}] + \sum_{j'=j+1}^{{}^{A}N_m} k_{j'j}^{s}[{}^{A}O_3^*(E_{j'})][\mathrm{M}], \quad 1 \leqslant j \leqslant {}^{A}N_m, \tag{A4}$$

where the first two terms describe formation and decay of this metastable state (number j), the third and fourth terms describe its stabilization onto all bound and lower-lying metastable states (up to $j-1$), respectively, while the last term describes stabilization of the upper-lying metastable states (starting at $j+1$ and going up) onto this metastable state. The rate coefficients for formation and decay are found from Eqs. (26) and (27). For the metastable states in channel B at energies above ^{B}ZPE the master equation is

$$\frac{d[{}^{B}\mathrm{O}_3^*(E_j)]}{dt} = k_j^f[{}^{B}\mathrm{O}][{}^{B}\mathrm{O}_2] - k_j^d[{}^{B}\mathrm{O}_3^*(E_j)] - \sum_{i=1}^{{}^{B}N_b} k_{ji}^s[{}^{B}\mathrm{O}_3^*(E_j)][\mathrm{M}] - \sum_{j'=1}^{{}^{B}N_\Delta} k_{jj'}^s[{}^{B}\mathrm{O}_3^*(E_j)] \times[\mathrm{M}] - \sum_{j'=1}^{j-1} k_{jj'}^s[{}^{B}\mathrm{O}_3^*(E_j)][\mathrm{M}] + \sum_{j'=j+1}^{{}^{B}N_m} k_{j'j}^s[{}^{B}\mathrm{O}_3^*(E_{j'})][\mathrm{M}], \quad 1 \leqslant j \leqslant {}^{B}N_m, \tag{A5}$$

where an additional term describes transitions onto the metastable states in the ΔZPE part of spectrum. However, for the metastable states in channel B at energies below the ^{B}ZPE the master equation is

$$\frac{d[{}^{\Delta}\mathrm{O}_3^*(E_j)]}{dt} = k_j^f[{}^{A}\mathrm{O}][{}^{A}\mathrm{O}_2] - k_j^d[{}^{\Delta}\mathrm{O}_3^*(E_j)] - \sum_{i=1}^{{}^{B}N_b} k_{ji}^s[{}^{\Delta}\mathrm{O}_3^*(E_j)][\mathrm{M}] - \sum_{j'=1}^{j-1} k_{jj'}^s[{}^{\Delta}\mathrm{O}_3^*(E_j)] \times[\mathrm{M}] + \sum_{j'=j+1}^{{}^{B}N_\Delta} k_{j'j}^s[{}^{\Delta}\mathrm{O}_3^*(E_{j'})][\mathrm{M}] + \sum_{j'=1}^{{}^{B}N_m} k_{j'j}^s[{}^{B}\mathrm{O}_3^*(E_{j'})][\mathrm{M}], \quad 1 \leqslant j \leqslant {}^{B}N_\Delta. \tag{A6}$$

Note that these states are formed from and decay to channel A. Thus, we should use $k_j^f = {}^{A}K_j k_j^d$ for these states.

Assuming the steady state conditions for every metastable state

$$\frac{d[{}^{A}\mathrm{O}_3^*(E_j)]}{dt} \approx 0, \quad \frac{d[{}^{B}\mathrm{O}_3^*(E_j)]}{dt} \approx 0, \quad \frac{d[{}^{\Delta}\mathrm{O}_3^*(E_j)]}{dt} \approx 0 \tag{A7}$$

we can find from Eqs. (A4)–(A6) the concentrations of all the metastable species, which then allows us to rewrite Eqs. (A2) and (A3) in the following form:

$$\frac{d[{}^{A}\mathrm{O}_3(E_i)]}{dt} = [{}^{A}\mathrm{O}][{}^{A}\mathrm{O}_2][\mathrm{M}]{}^{AA}\kappa_i, \tag{A8}$$

$$\frac{d[{}^{B}\mathrm{O}_3(E_i)]}{dt} = [{}^{A}\mathrm{O}][{}^{A}\mathrm{O}_2][\mathrm{M}]{}^{A\Delta}\kappa_i + [{}^{B}\mathrm{O}][{}^{B}\mathrm{O}_2][\mathrm{M}]{}^{BB}\kappa_i + [{}^{B}\mathrm{O}][{}^{B}\mathrm{O}_2][\mathrm{M}]{}^{B\Delta}\kappa_i, \tag{A9}$$

where the third-order rate coefficients have been introduced as

$${}^{AA}\kappa_i \equiv \sum_{j=1}^{{}^{A}N_m} {}^{AA}P_j k_{ji}^s, \quad {}^{A\Delta}\kappa_i \equiv \sum_{j=1}^{{}^{B}N_\Delta} {}^{A\Delta}P_j k_{ji}^s,$$

$${}^{BB}\kappa_i \equiv \sum_{j=1}^{{}^{B}N_m} {}^{BB}P_j k_{ji}^s, \quad {}^{B\Delta}\kappa_i \equiv \sum_{j=1}^{{}^{B}N_\Delta} {}^{B\Delta}P_j k_{ji}^s. \tag{A10}$$

The values of ${}^{AA}P_j$, ${}^{A\Delta}P_j$, ${}^{BB}P_j$, and ${}^{B\Delta}P_j$ are computed using recurrent formula starting at the upper states and going down,

$${}^{AA}P_j = \frac{{}^{A}K_j k_j^d + [\mathrm{M}]\Sigma_{j'=j+1}^{{}^{A}N_m} {}^{AA}P_{j'} k_{j'j}^s}{k_j^d + [\mathrm{M}]\left(\Sigma_{i=1}^{{}^{A}N_b} k_{ji}^s + \Sigma_{j'=1}^{j-1} k_{jj'}^s\right)}, \quad 1 \leqslant j \leqslant {}^{A}N_m, \tag{A11}$$

$${}^{A\Delta}P_j = \frac{{}^{A}K_j k_j^d + [\mathrm{M}]\Sigma_{j'=j+1}^{{}^{B}N_\Delta} {}^{A\Delta}P_{j'} k_{j'j}^s}{k_j^d + [\mathrm{M}]\left(\Sigma_{i=1}^{{}^{B}N_b} k_{ji}^s + \Sigma_{j'=1}^{j-1} k_{jj'}^s\right)}, \quad 1 \leqslant j \leqslant {}^{B}N_\Delta, \tag{A12}$$

$${}^{BB}P_j = \frac{{}^{B}K_j k_j^d + [\mathrm{M}]\Sigma_{j'=j+1}^{{}^{B}N_m} {}^{BB}P_{j'} k_{j'j}^s}{k_j^d + [\mathrm{M}]\left(\Sigma_{i=1}^{{}^{B}N_b} k_{ji}^s + \Sigma_{j'=1}^{{}^{B}N_\Delta} k_{jj'}^s + \Sigma_{j'=1}^{j-1} k_{jj'}^s\right)}, \quad 1 \leqslant j \leqslant {}^{B}N_m, \tag{A13}$$

$${}^{B\Delta}P_j = \frac{[\mathrm{M}]\left(\Sigma_{j'=j+1}^{{}^{B}N_\Delta} {}^{B\Delta}P_{j'} k_{j'j}^s + \Sigma_{j'=1}^{{}^{B}N_m} {}^{BB}P_{j'} k_{j'j}^s\right)}{k_j^d + [\mathrm{M}]\left(\Sigma_{i=1}^{{}^{B}N_b} k_{ji}^s + \Sigma_{j'=1}^{j-1} k_{jj'}^s\right)}, \quad 1 \leqslant j \leqslant {}^{B}N_\Delta. \tag{A14}$$

Finally, the rate of ozone formation can be expressed as

$$\begin{aligned}\mathrm{rate} &= [{}^{A}\mathrm{O}][{}^{A}\mathrm{O}_2][\mathrm{M}]\sum_{i=1}^{{}^{A}N_b} {}^{AA}\kappa_i + [{}^{A}\mathrm{O}][{}^{A}\mathrm{O}_2][\mathrm{M}]\sum_{i=1}^{{}^{B}N_b} {}^{A\Delta}\kappa_i \\ &\quad + [{}^{B}\mathrm{O}][{}^{B}\mathrm{O}_2][\mathrm{M}]\sum_{i=1}^{{}^{B}N_b} {}^{BB}\kappa_i + [{}^{B}\mathrm{O}][{}^{B}\mathrm{O}_2][\mathrm{M}]\sum_{i=1}^{{}^{B}N_b} {}^{B\Delta}\kappa_i \\ &= [{}^{A}\mathrm{O}][{}^{A}\mathrm{O}_2][\mathrm{M}]{}^{A}\kappa + [{}^{B}\mathrm{O}][{}^{B}\mathrm{O}_2][\mathrm{M}]{}^{B}\kappa,\end{aligned} \tag{A15}$$

where the channel-specific third order rate coefficients were introduced as

$${}^{A}\kappa \equiv \sum_{i=1}^{{}^{A}N_b} {}^{AA}\kappa_i + \sum_{i=1}^{{}^{B}N_b} {}^{A\Delta}\kappa_i,$$

$${}^{B}\kappa \equiv \sum_{i=1}^{{}^{B}N_b} {}^{BB}\kappa_i + \sum_{i=1}^{{}^{B}N_b} {}^{B\Delta}\kappa_i. \tag{A16}$$

These are used to calculate the ratio $R = {}^{B}\kappa/{}^{A}\kappa$ for the isotope effect.

There are two interesting limiting cases when the Eqs. (A11)–(A14) can be simplified. If all the metastable states are broad

$$\Gamma_j = k_j^d \gg \begin{cases} k_{j,j-1}^s[\mathrm{M}], \\ \dfrac{K_{j+1}}{K_j} k_{j+1,j}^s[\mathrm{M}], \end{cases} \tag{A17}$$

we obtain

$$\begin{aligned} {}^{AA}P_j &\approx {}^{A}K_j, \quad {}^{A\Delta}P_j \approx {}^{A}K_j, \\ {}^{BB}P_j &\approx {}^{B}K_j, \quad {}^{B\Delta}P_j \approx 0. \end{aligned} \tag{A18}$$

Expressions for ${}^{A}\kappa$ and ${}^{B}\kappa$ in this limit also become very simple; they are given in the text as Eqs. (29) and (30).

If the resonances in the ΔZPE range are narrow (an opposite limit),

$$\Gamma_j = k_j^d \ll k_{j,j-1}^s[\mathrm{M}], \tag{A19}$$

we obtain for these states

$$\begin{aligned} {}^{A\Delta}P_j &\sim 0, \\ {}^{B\Delta}P_j &\approx \frac{\sum_{j'=j+1}^{{}^{B}N_\Delta} {}^{B\Delta}P_{j'} k_{j'j}^s + \sum_{j'=1}^{{}^{B}N_m} {}^{BB}P_{j'} k_{j'j}^s}{\sum_{i=1}^{{}^{B}N_b} k_{ji}^s + \sum_{j'=1}^{j-1} k_{jj'}^s}. \end{aligned} \tag{A20}$$

In this limit the expression for ${}^{A}\kappa$ simplifies to Eq. (31) given in the text. The expression for ${}^{B}\kappa$ is somewhat harder to derive. Using Eqs. (A19) and (A20) for narrow resonances in the ΔZPE range and Eqs. (A17) and (A18) for all other broad resonances we obtain from Eqs. (A16) and (A10)

$${}^{B}\kappa \approx \sum_{j=1}^{{}^{B}N_m} {}^{B}K_j \sum_{i=1}^{{}^{B}N_b} k_{ji}^s + \sum_{j=1}^{{}^{B}N_\Delta} {}^{B\Delta}P_j \sum_{i=1}^{{}^{B}N_b} k_{ji}^s. \tag{A21}$$

In the second term of Eq. (A21) which represents ${}^{B\Delta}\kappa$ we have to expand the sum over j like this,

$$\begin{aligned} {}^{B\Delta}\kappa \approx \sum_{j=1}^{{}^{B}N_\Delta} {}^{B\Delta}P_j \sum_{i=1}^{{}^{B}N_b} k_{ji}^s &= {}^{B\Delta}P_1 \sum_{i=1}^{{}^{B}N_b} k_{1i}^s \\ &+ {}^{B\Delta}P_2 \sum_{i=1}^{{}^{B}N_b} k_{2i}^s + {}^{B\Delta}P_3 \sum_{i=1}^{{}^{B}N_b} k_{3i}^s + \cdots . \end{aligned} \tag{A22}$$

Using ansatz Eq. (A20) for ${}^{B\Delta}P_1$ in the first term of (A22) we obtain

$$\begin{aligned} {}^{B\Delta}\kappa = \frac{\sum_{j'=2}^{{}^{B}N_\Delta} {}^{B\Delta}P_{j'} k_{j'1}^s + \sum_{j'=1}^{{}^{B}N_m} {}^{B}K_{j'} k_{j'1}^s}{\sum_{i=1}^{{}^{B}N_b} k_{1i}^s} \sum_{i=1}^{{}^{B}N_b} k_{1i}^s + {}^{B\Delta}P_2 \\ \times \sum_{i=1}^{{}^{B}N_b} k_{2i}^s + {}^{B\Delta}P_3 \sum_{i=1}^{{}^{B}N_b} k_{3i}^s + \cdots . \end{aligned} \tag{A23}$$

Note that in the first term of Eq. (A23) the sum over the bound states cancels out and only the nominator survives. Expanding the first term in the nominator we obtain

$$\begin{aligned} {}^{B\Delta}\kappa = \sum_{j'=1}^{{}^{B}N_m} {}^{B}K_{j'} k_{j'1}^s + {}^{B\Delta}P_2 k_{21}^s + {}^{B\Delta}P_3 k_{31}^s \\ + \cdots + {}^{B\Delta}P_2 \sum_{i=1}^{{}^{B}N_b} k_{2i}^s + {}^{B\Delta}P_3 \sum_{i=1}^{{}^{B}N_b} k_{3i}^s + \cdots . \end{aligned} \tag{A24}$$

In Eq. (A24) we can combine the terms with ${}^{B\Delta}P_2$, ${}^{B\Delta}P_3$, etc., and use Eq. (A20) again; now for ${}^{B\Delta}P_2$,

$$\begin{aligned} {}^{B\Delta}\kappa = \sum_{j'=1}^{{}^{B}N_m} {}^{B}K_{j'} k_{j'1}^s \\ + \frac{\sum_{j'=3}^{{}^{B}N_\Delta} {}^{B\Delta}P_{j'} k_{j'2}^s + \sum_{j'=1}^{{}^{B}N_m} {}^{B}K_{j'} k_{j'2}^s}{\sum_{i=1}^{{}^{B}N_b} k_{2i}^s + k_{21}^s} \left(\sum_{i=1}^{{}^{B}N_b} k_{2i}^s + k_{21}^s \right) \\ + {}^{B\Delta}P_3 \left(\sum_{i=1}^{{}^{B}N_b} k_{3i}^s + k_{31}^s \right) + \cdots . \end{aligned} \tag{A25}$$

Note that in the second term of Eq. (A25) the sum over the bound states cancels out again. Repeating this procedure ${}^{\Delta}N_m$ times we obtain

$$\begin{aligned} {}^{B\Delta}\kappa &= \sum_{j'=1}^{{}^{B}N_m} {}^{B}K_{j'} k_{j'1}^s + \sum_{j'=1}^{{}^{B}N_m} {}^{B}K_{j'} k_{j'2}^s + \cdots + \sum_{j'=1}^{{}^{B}N_m} {}^{B}K_{j'} k_{j',{}^{\Delta}N_m}^s \\ &= \sum_{j=1}^{{}^{B}N_m} {}^{B}K_j \sum_{i=1}^{{}^{\Delta}N_m} k_{ji}^s. \end{aligned} \tag{A26}$$

Combining this result with the first term in Eq. (A21) we obtain Eq. (32) given in the text for ${}^{B}\kappa$.

[1] J. Guenther, D. Krankowsky, and K. Mauersberger, Chem. Phys. Lett. **324**, 31 (2000).
[2] F. A. Lindemann, Trans. Faraday Soc. **17**, 598 (1922).
[3] R. E. Roberts, R. B. Bernstein, and C. F. Curtiss, J. Chem. Phys. **50**, 5163 (1969).
[4] R. T Pack, R. B. Walker, and B. K. Kendrick, J. Chem. Phys. **109**, 6701 (1998).
[5] M. H. Thimens and J. E. Heidenreich III, Science **219**, 1073 (1983).
[6] M. H. Thiemens, Science **283**, 341 (1999).
[7] K. Mauersberger, B. Erbacher, D. Krankowsky, J. Gunther, and R. Nickel, Science **283**, 370 (1999).
[8] C. Janssen, J. Guenther, K. Mauersberger, and D. Krankowsky, Phys. Chem. Chem. Phys. **3**, 4718 (2001).
[9] J. Guenther, B. Erbacher, D. Krankowsky, and K. Mauersberger, Chem. Phys. Lett. **306**, 209 (1999).
[10] K. Mauersberger, D. Krankowsky, C. Janssen, and R. Schinke, Adv. At., Mol., Opt. Phys. **50**, 1 (2005).
[11] B. C. Hathorn and R. A. Marcus, J. Chem. Phys. **111**, 4087 (1999).
[12] B. C. Hathorn and R. A. Marcus, J. Chem. Phys. **113**, 9497 (2000).
[13] B. C. Hathorn and R. A. Marcus, J. Phys. Chem. A **105**, 5586 (2001).
[14] Y. Q. Gao and R. A. Marcus, J. Chem. Phys. **116**, 137 (2002).
[15] Y. Q. Gao, W.-C. Chen, and R. A. Marcus, J. Chem. Phys. **117**, 1536 (2002).
[16] D. Charlo and D. C. Clary, J. Chem. Phys. **117**, 1660 (2002).
[17] T. A. Baker and G. I. Gellene, J. Chem. Phys. **117**, 7603 (2002).
[18] D. Babikov, B. K. Kendrick, R. B. Walker, P. Fleurat-Lesard, R. Schinke, and R. T Pack, J. Chem. Phys. **118**, 6298 (2003).
[19] D. Babikov, B. K. Kendrick, R. B. Walker, P. Fleurat-Lesard, R. Schinke, and R. T Pack, J. Chem. Phys. **119**, 2577 (2003).
[20] D. Babikov, B. K. Kendrick, R. B. Walker, R. Schinke, and R. T Pack, Chem. Phys. Lett. **372**, 686 (2003).
[21] H.-S. Lee and J. C. Light, J. Chem. Phys. **120**, 5859 (2004).

[22] R. Siebert, P. Fleurat-Lessard, M. Bittererova, S. C. Farantos, and R. Schinke, J. Chem. Phys. **116**, 9749 (2002).
[23] P. Fleurat-Lessard, S. Yu. Grebenshchikov, R. Siebert, R. Schinke, and N. Halberstadt, J. Chem. Phys. **118**, 610 (2003).
[24] R. Schinke, P. Fleurat-Lessard, and S. Yu. Grebenshchikov, Phys. Chem. Chem. Phys. **5**, 1966 (2003).
[25] R. Schinke and P. Fleurat-Lessard, J. Chem. Phys. **122**, 094317 (2005).
[26] R. Schinke, S. Yu. Grebenshchikov, M. V. Ivanov, and P. Fleurat-Lessard, Annu. Rev. Phys. Chem. **57**, 625 (2006).
[27] K. Luther, K. Oum, and J. Troe, Phys. Chem. Chem. Phys. **7**, 2764 (2005).
[28] T. Xie and J. M. Bowman, Chem. Phys. Lett. **412**, 131 (2005).
[29] E. Vetoshkin and D. Babikov, J. Chem. Phys. **125**, 024302 (2006).
[30] E. J. Heller, J. Chem. Phys. **75**, 2923 (1981).
[31] M. F. Herman and E. Kluk, Chem. Phys. **91**, 27 (1984).
[32] E. Kluk, M. F. Herman, and H. L. Davis, J. Chem. Phys. **84**, 326 (1986).
[33] M. F. Herman, Chem. Phys. Lett. **275**, 445 (1997).
[34] V. S. Batista and W. H. Miller, J. Chem. Phys. **108**, 498 (1997).
[35] F. Grossmann, Phys. Rev. A **57**, 3256 (1998).
[36] K. G. Kay, J. Chem. Phys. **101**, 2250 (1994).
[37] Z. Li and R. B. Gerber, J. Chem. Phys. **99**, 8637 (1993).
[38] A. Walton and D. Manolopoulous, Mol. Phys. **87**, 961 (1996).
[39] F. Grossmann, Chem. Phys. Lett. **262**, 470 (1996).
[40] Vl. G. Tyuterev, S. Tashkun, D. W. Schwenke, P. Jensen, T. Cours, A. Barbe, and M. Jacon, Chem. Phys. Lett. **316**, 271 (2000).
[41] P. Krupernie, J. Phys. Chem. Ref. Data **1**, 423 (1972).
[42] M. W. Chase, Jr., C. A. Davies, J. R. Downey, Jr., D. J. Frurip, R. A. McDonald, and A. N. Syverud, J. Phys. Chem. Ref. Data **14**, 1 (1985).
[43] M. V. Ivanov, H. Zhu, and R. Schinke, J. Chem. Phys. **126**, 054304 (2007).
[44] J. S. Francisco, J. R. Lyons, and I. H. Williams, J. Chem. Phys. **123**, 54302 (2005).
[45] K. A. Peterson, J. R. Lyons, and J. S. Francisco, J. Chem. Phys. **125**, 084314 (2006).
[46] R. Kosloff, J. Phys. Chem. **92**, 2087 (1988).
[47] S. K. Gray, J. Chem. Phys. **96**, 6543 (1992).
[48] E. Pollak, in *Intramolecular Dynamics*, edited by J. Jortner and B. Pullman (Reidel, Dordrecht, 1982), p. 1.
[49] D. C. Clary and J. N. L. Connor, Chem. Phys. Lett. **94**, 81 (1983).
[50] J. M. Bowman and B. Gazdy, J. Phys. Chem. **93**, 5129 (1989).
[51] G. Ma and H. Guo, J. Chem. Phys. **111**, 4032 (1999).
[52] R. T Pack, R. B. Walker, and B. K. Kendrick, J. Chem. Phys. **109**, 6714 (1998).
[53] H. Hippler, R. Rahn, and J. Troe, J. Chem. Phys. **93**, 6560 (1990).